Engineering 28 (2023) 69–78

Contents lists available at ScienceDirect

Engineering

journal homepage: www.elsevier.com/locate/eng

Research
Material Science and Engineering—Article

Highly Conductive Proton Selectivity Membrane Enabled by Hollow Carbon Sieving Nanospheres for Energy Storage Devices

Kang Huang [a,#], Shuhao Lin [a,#], Yu Xia [a], Yongsheng Xia [a], Feiyan Mu [a], Yuqin Lu [a], Hongyan Cao [a], Yixing Wang [b], Weihong Xing [a], Zhi Xu [b,*]

[a] State Key Laboratory of Materials-Oriented Chemical Engineering, College of Chemical Engineering, Nanjing Tech University, Nanjing 211816, China
[b] State Key Laboratory of Chemical Engineering, School of Chemical Engineering, East China University of Science and Technology, Shanghai 200237, China

ARTICLE INFO

Article history:
Received 8 July 2022
Revised 3 November 2022
Accepted 27 November 2022
Available online 17 March 2023

Keywords:
Ion conductive membrane
Hollow carbon sieving nanosphere
Proton transport channel
Flow battery

ABSTRACT

Ion conductive membranes (ICMs) with highly conductive proton selectivity are of significant importance and greatly desired for energy storage devices. However, it is extremely challenging to construct fast proton-selective transport channels in ICMs. Herein, a membrane with highly conductive proton selectivity was fabricated by incorporating porous carbon sieving nanospheres with a hollow structure (HCSNs) in a polymer matrix. Due to the precise ion sieving ability of the microporous carbon shells and the fast proton transport through their accessible internal cavities, this advanced membrane presented a proton conductivity (0.084 $S{\cdot}cm^{-1}$) superior to those of a commercial Nafion 212 (N212) membrane (0.033 $S{\cdot}cm^{-1}$) and a pure polymer membrane (0.049 $S{\cdot}cm^{-1}$). The corresponding proton selectivity of the membrane (6.68×10^5 $S{\cdot}min{\cdot}cm^{-3}$) was found to be enhanced by about 5.9-fold and 4.3-fold, respectively, compared with those of the N212 membrane (1.13×10^5 $S{\cdot}min{\cdot}cm^{-3}$) and the pure membrane (1.56×10^5 $S{\cdot}min{\cdot}cm^{-3}$). Low-field nuclear magnetic resonance (LF-NMR) clearly revealed the fast proton-selective transport channels enabled by the HCSNs in the polymeric membrane. The proposed membrane exhibited an outstanding energy efficiency (EE) of 84% and long-term stability over 1400 cycles with a 0.065% capacity decay per cycle at 120 $mA{\cdot}cm^{-2}$ in a typical vanadium flow battery (VFB) system.

1. Introduction

Developing large-scale energy conversion and storage technologies is becoming increasingly critical for the utilization of clean and renewable energies [1–6]. As a core component in energy conversion and storage devices such as fuel cells and flow batteries [7], ion conductive membranes (ICMs) ensure fast proton transport while providing precise sieving of reactive species [8–12]. At present, the perfluorosulfonic polymer membranes represented by Nafion membranes are widely used in this field due to their good chemical stability and proton conductivity. However, their low ion selectivity and high cost have severely restricted their further application in electrochemical energy technologies [13,14]. Therefore, the development of cost-efficient non-perfluorosulfonic membranes with high performance has attracted widespread attention.

Recently, aromatic polymers such as sulfonated poly(ether ether ketone) (SPEEK) have been extensively researched as ICMs due to their easy process preparation, low cost, good mechanical stability, controllable proton conductivity, and strong resistance to reactive species permeation. These potential materials are expected to replace Nafion membranes, because they can be easily fabricated on a large scale [15,16]. To further improve the various capabilities of these membranes, modification strategies based on the incorporation of inorganic nanomaterials into a polymeric matrix are a potential method [17,18]. Studies have reported on the introduction of guest inorganic fillers, which can achieve improved proton selectivity [19,20], and on the interfacial interactions between the rigid inorganic materials and the polymer matrix, which can enhance the dimensional stability and mechanical properties of the hybrid membranes [21,22].

However, traditional inorganic materials such as TiO_2 [23], SiO_2 [24], and ZrO_2 [25] act as physical barriers against ion transport, including the transport of reactive ions and protons. Moreover, these fillers cannot offset the sacrifice of proton conductivity, even when they are functionalized. Over the years, researchers have

* Corresponding author.
E-mail address: zhixu@ecust.edu.cn (Z. Xu).
# These authors contributed equally to this work.

https://doi.org/10.1016/j.eng.2022.11.008

attempted to apply porous materials to both enhance ion sieving and ensure proton transfer by utilizing pore size exclusion. For example, metal–organic frameworks (MOFs) and covalent-organic frameworks (COFs) are commonly considered to be excellent proton-conductive materials due to their intrinsic merits such as internal interconnected channels and tunable pore size [26–29]. Nevertheless, numerous realistic results have shown that hybrid membranes with MOFs and COFs still exhibit undesirable proton conductivity due to their tortuous internal space. Based on this analysis, a reliable idea could be to prepare a porous material with a precise ion sieving shell and hollow internal structure; the microporous shell could improve the ion sieving ability, while the internal cavity would act as an ultrafast proton transport channel without any resistance [30–34].

In this work, hollow carbon sieving nanospheres (HCSNs) were successfully applied as a dispersion phase in a SPEEK matrix to construct fast proton-selective transport channels, thanks to their unique architecture, which includes a carbon shell layer with a porous structure and an internal void (Fig. 1(a)). The porous carbon shell layer effectively impedes the diffusion of large active materials [35,36], such as vanadium ions, while the hollow nanostructures provide extra-fast proton transport channels in the membrane, resulting in an enhancement of the proton transfer rate. In addition, a large amount of water molecules can be stored in the inner space of the HCSNs, which further improves the proton transport ability by means of the vehicular mechanism [37,38]. Low-field nuclear magnetic resonance (LF-NMR) showed plentiful water molecule transfer channels through the internal cavity of the HCSNs. The obtained membranes exhibit increased proton conductivity and proton selectivity compared with a SPEEK membrane. Moreover, both the chemical stability and tensile strength of these hybrid membranes are reinforced by the special structure

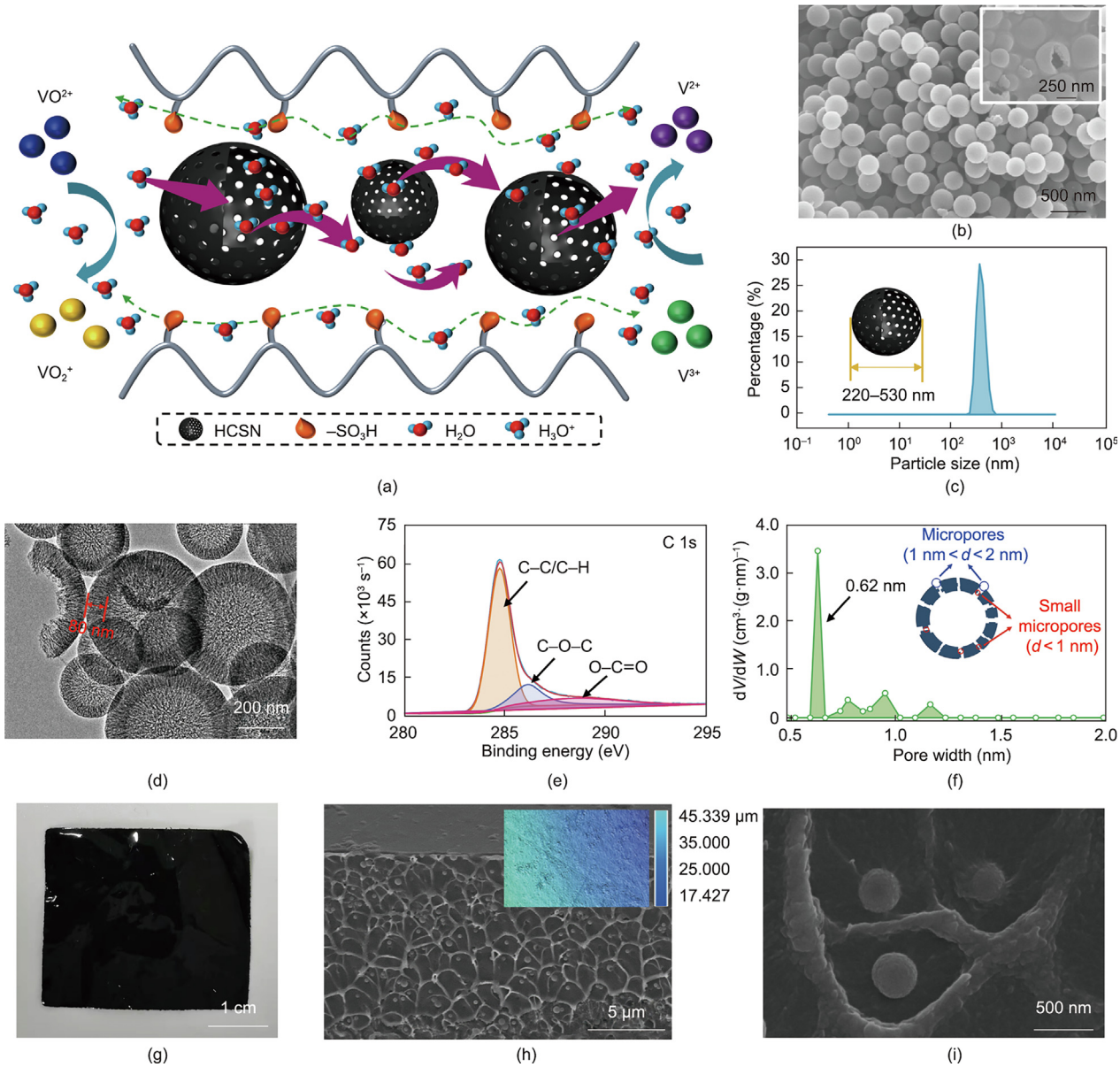

Fig. 1. Characterizations of HCSNs and hybrid membranes. (a) Schematic illustration of the proton transport mechanism in a polymer matrix embedded with HCSNs. (b–f) Characterizations of HCSNs: (b) scanning electron microscope (SEM) image of HCSNs (inset shows a close-up SEM image of HCSNs); (c) particle size distribution; (d) transmission electron microscope (TEM) image of intact and broken HCSNs; (e) X-ray photoelectron spectroscopy (XPS) C 1s spectra; (f) micropore size distribution and schematic illustration of pore structure. (g–i) Characterizations of the SPEEK/HCSN membrane (mass loading: 3% (w/w)): (g) digital photo; (h) cross-section SEM image (inset shows an image of the corresponding white light interferometer); (i) close-up SEM image of the HCSN/polymer interface.

of the HCSNs. Hence, our research provides a feasible strategy for the preparation of a highly conductive proton selectivity membrane for future application in energy conversion and storage.

2. Materials and methods

2.1. Materials

Poly(ether ether ketone) (PEEK; Victrex™ PEEK 450G) was purchased from Nanjing Shousu Special Engineering Plastic Products Co., Ltd., China; *N*,*N*-dimethylformamide (DMF) was purchased from Shanghai Aladdin Bio-Chem Technology Co., Ltd., China; sulfuric acid (H_2SO_4, 98% (w/w)) was purchased from Yonghua Chemical Co., Ltd., China; $VOSO_4{\cdot}3H_2O$ was purchased from Nanjing Jingruijiuan Biotechnology Co., Ltd., China; and carbon spheres were supplied by Nanjing XFNANO Materials Tech Co., Ltd., China.

2.2. Preparation of SPEEK/HCSN hybrid membranes

First, 25 g of PEEK was added to 250 mL of H_2SO_4 (98%) and the mixture was reacted under magnetic stirring at 50 °C for 5 h. Subsequently, the mixture was poured into ice-cold water with continuous mechanical stirring to form precipitated SPEEK. The product was then washed with deionized water until the pH was almost 7; it was then dried, first at 60 °C and then in a vacuum oven at 100 °C for 24 h.

The SPEEK/HCSN hybrid membrane was prepared using the solution casting method. Firstly, 1.5 g of SPEEK and *X* mg of HCSN powder (where *X* = 15, 30, 45, 60, or 75) were dissolved in 10 mL of DMF. The mixture was then ball-milled for 24 h and sonicated for 30 min to form a homogeneous mixture. To remove the agglomerated large particles in the mixture, centrifuging was carried out at a speed of 12 000 $r{\cdot}min^{-1}$ for 10 min. The resultant solution was poured onto a flat glass, dried in an oven at 60 °C, and further dried under vacuum at 100 °C for 12 h to form a hybrid membrane. After being peeled off from the glass, the hybrid membrane was immersed in a 1 $mol{\cdot}L^{-1}$ H_2SO_4 solution for 24 h to achieve the activation process. Excess deionized water was then employed to wash off the residual acid on the surface of the membrane, and the membrane was stored in fresh deionized water for later use.

2.3. Characterization

2.3.1. Instrumentation

The micromorphologies of the hollow carbon sphere powder and the membranes were characterized by means of a field emission scanning electron microscope (FE-SEM; Hitachi S4800, Hitachi, Ltd., Japan). The operating parameters were a voltage of 3 kV and a current of 5 μA. Energy-dispersive X-ray (EDX) analysis mapping results were obtained to analyze the elemental composition of the HCSNs and of a cross-section of the hybrid membrane. Transmission electron microscope (TEM) images were obtained to observe the hollow structure of the HCSN powder. Samples were measured by means of a JEM 2100 (JEOL Ltd., Japan) electron microscope. The Fourier-transform infrared (FT-IR) spectrum of the HCSNs was recorded using a FT-IR spectrometer (Nicolet 8700, Thermo Fisher Scientific, USA) between 4000 and 500 cm^{-1}. The particle size distribution of the HCSNs was analyzed by means of a zeta potentiometer (ZS90, Malvern, UK). A white light interferometer (laser microscope VK-1050, Keyence, Japan) was employed and the contact angles were measured (using a Dropmeter A-100) to characterize the roughness and hydrophilicity, respectively, of the membrane surface. A thermogravimetric (TG) analysis of the samples was performed using a simultaneous thermal analyzer (STA 449F3, NETZSCH, Germany) at a heating rate of 10 $°C{\cdot}min^{-1}$ under an air atmosphere. The micropore size distribution of the HCSN powder was measured via nitrogen (N_2) adsorption–desorption isotherms using a Micromeritics ASAP 2460 (Micromeritics Instrument Corp., USA) in a liquid nitrogen environment. The arrangement of the polymer chains within the hybrid membrane was qualitatively analyzed by X-ray diffraction (XRD; Rigaku Miniflex 600 diffractometer, Japan) with Cu Kα radiation at a scan rate of 10 $°C{\cdot}min^{-1}$ in the range of 5°–50° (2θ). LF-NMR (MesoMR23/12-060H-I, Suzhou Toptest Instrument Co., Ltd., China) was employed to characterize the sub-nanometer and nanometer confined water within the hybrid membranes.

2.3.2. Water uptake and swelling ratio

Membranes were cut into samples of the same size (25 mm × 10 mm) to measure the water uptake (WU) and swelling ratio (SR). First, the samples were immersed in deionized water for 24 h. Subsequently, filter paper was used to absorb the moisture from the membrane surface and rapidly cause the wet membranes to become relatively dry. Then, the wet weights and lengths of the membrane samples were recorded. Second, the measured wet membranes were dried in a vacuum oven at 100 °C for 12 h. After the drying process, the weights and lengths of the dry membrane samples were recorded. For each type of membrane, three repetitions were carried out, and the average values were obtained. The WU and SR were calculated by Eqs. (1) and (2), respectively:

$$\mathrm{WU} = \frac{W_{\mathrm{wet}} - W_{\mathrm{dry}}}{W_{\mathrm{dry}}} \times 100\% \tag{1}$$

$$\mathrm{SR} = \frac{L_{\mathrm{wet}} - L_{\mathrm{dry}}}{L_{\mathrm{dry}}} \times 100\% \tag{2}$$

where W_{wet} (g) and W_{dry} (g) represent the weight of the membranes in the wet and dry state, respectively; and L_{wet} (mm) and L_{dry} (mm) are the lengths of the wet and dry membranes, respectively.

2.3.3. Ion exchange capacity

The ion exchange capacity (IEC) of the membranes was tested by means of potentiometric titration. Before the test, the wet membrane samples were fully dried, and the weights of the dry membrane samples were recorded. Then, 1 $mol{\cdot}L^{-1}$ H_2SO_4 solution was poured into the beaker containing the samples and was left for 24 h. After the residual acid on the surface of the membrane samples was removed, the samples were immersed in 50 mL of saturated NaCl solution for 24 h. The resulting solution was then titrated with 0.3 $mol{\cdot}L^{-1}$ NaOH solution. The IEC value was calculated according to Eq. (3):

$$\mathrm{IEC} = \frac{c_{\mathrm{NaOH}} \times V_{\mathrm{NaOH}}}{W_{\mathrm{dry}}} \tag{3}$$

where c_{NaOH} ($mol{\cdot}L^{-1}$) is the concentration of the NaOH solution and V_{NaOH} (mL) is the consumed volume of the NaOH solution.

2.3.4. Mechanical properties

The mechanical properties of the samples were measured with a universal machine at a tensile speed of 5 $mm{\cdot}min^{-1}$. The water on the surface of the samples was wiped with filter paper; then, the samples were cut into long strips of 50 mm × 10 mm. To reduce the testing error, three sample measurements were carried out for each membrane, and the average tensile strength of each sample was obtained from the resulting data. The tensile strength (T) was calculated using Eq. (4):

$$T = \frac{F_{\max}}{WL} \tag{4}$$

where $F_{\max}$ (N) is the maximum tension, and W (mm) and L (μm) are the width and thickness of the membranes, respectively.

2.3.5. Chemical stability

The chemical stability of the membrane was evaluated by determining the weight loss of the membrane and the reduction of VO_2^+ to VO^{2+} after the membrane was immersed in the strong oxidation VO_2^+ catholyte (0.1 mol·L^{-1} VO_2^+ in 3.0 mol·L^{-1} H_2SO_4 solution) for 30 days. The concentration of VO^{2+} ions was determined by measuring the absorbance at 760 nm with an ultraviolet visible (UV–Vis) spectrophotometer (Lambda 950, PerkinElmer, USA). The reduction of VO_2^+ to VO^{2+} were calculated using Eq. (5):

$$\text{Reduction of } VO_2^+ \text{ to } VO^{2+} = \frac{c_{VO^{2+}}}{c_{VO_2^+}} \times 100\% \tag{5}$$

where $c_{VO^{2+}}$ (mol·L^{-1}) and $c_{VO_2^+}$ (mol·L^{-1}) are the VO^{2+} concentration of the immersed solution after 30 days and the concentration of the initial VO_2^+ solution, respectively.

2.3.6. Area resistance and proton conductivity

The area resistance (AR) of the membrane was measured using an electrochemical impedance spectroscopy workstation with the alternating current (AC) impedance method. The sample was sandwiched between two round titanium tablets and fixed in place with a button battery clamp. The proton conductivity of the membrane was measured using a simple method reported by Li's group [39], shown as Eq. (6):

$$\sigma = \frac{L}{R \times A} \tag{6}$$

where σ (S·cm^{-1}) is the proton conductivity of the membrane, R (Ω) is the resistance of the sample, and A (cm^2) is the effective area of the sample, which is consistent with the area of one round titanium tablet.

The AR of the membrane (R_A) was calculated using Eq. (7):

$$R_A = R \times A \tag{7}$$

All of the samples were pretreated in 3 mol·L^{-1} H_2SO_4 solution overnight.

2.3.7. Permeability of VO^{2+} and proton selectivity

The permeability of the membrane to vanadium ions was tested in a diffusion cell separated by the membrane sample (with an effective area of about 1.77 cm^2), with two 50 mL half cells. The feed side was filled with 50 mL of 1.5 mol·L^{-1} $VOSO_4$ dissolved in 3.0 mol·L^{-1} H_2SO_4, while the permeation side was filled with the same volume of 1.5 mol·L^{-1} $MgSO_4$ dissolved in 3.0 mol·L^{-1} H_2SO_4 to balance the ion strength and reduce the osmotic pressure. Magnetic stirring was carried out continuously on both sides to reduce the concentration polarization. A specific volume was collected from the permeation side containing $MgSO_4$ solution every 12 h, and the same volume of 1.5 mol·L^{-1} $MgSO_4$/3.0 mol·L^{-1} H_2SO_4 was added back. The concentration of VO^{2+} was obtained by measuring the absorbance at 762 nm with a UV–Vis spectrophotometer. The permeability and proton selectivity were calculated according to Eqs. (8) and (9):

$$V_B \frac{d[c_B(t)]}{dt} = A\frac{P}{L}[c_A - c_B(t)] \tag{8}$$

$$S = \frac{\sigma}{P} \tag{9}$$

where V_B (mL) is the volume of one half cell; $c_B(t)$ (mol·L^{-1}) represents the concentration of VO^{2+} in the $MgSO_4$ compartment as a function of time t; c_A (mol·L^{-1}) is the initial vanadium concentration in the $VOSO_4$ compartment; P (cm^2·min^{-1}) is the vanadium ion permeability; and S (S·min·cm^{-3}) represents the proton selectivity.

2.3.8. VO^{2+} permeability properties

The Maxwell model was used to estimate the effective permeability of the spherical or near-spherical fillers within the hybrid membrane. The Maxwell model is given by Eq. (10):

$$D_{eff} = D_m\left[\frac{D_f + 2D_m - 2(D_m - D_f)\Phi_f}{D_f + 2D_m + (D_m - D_f)\Phi_f}\right] \tag{10}$$

where D_{eff} is the effective VO^{2+} permeability of the hybrid membrane; D_m and D_f are the intrinsic VO^{2+} permeability of the polymer matrix and the fillers, respectively; and Φ_f is the volume fraction of the fillers in the polymer matrix.

2.3.9. Vanadium flow battery single cell test

A home-made single cell was made, consisting of a membrane sandwiched between two pieces of carbon felt (with an effective area of 3.0 cm × 3.5 cm and a thickness of 5.0 mm), two graphite plate current collectors, and two acrylic endplates. All the carbon felt used in this work was activated by means of solution soaking and the high-temperature calcination method. The volume of electrolyte on both sides was 10 mL. The initial positive and negative electrolytes were composed of 1.5 mol·L^{-1} VO^{2+} and 1.5 mol·L^{-1} V^{3+} in 3 mol·L^{-1} H_2SO_4, respectively. The nitrogen atmosphere was continuously refreshed to prevent the vanadium ions from being oxidized by oxygen in the air during the test. The cut-off voltages were set at 1.7 and 0.8 V, and the current density ranged from 40 to 120 mA·cm^{-2} for the charge and discharge test. The coulomb efficiency (CE), energy efficiency (EE), and voltage efficiency (VE) of the vanadium flow battery (VFB) single cell were calculated using Eqs. (11)–(13).

$$CE = \frac{\text{Discharge capacity}}{\text{Charge capacity}} \times 100\% \tag{11}$$

$$EE = \frac{\text{Discharge energy}}{\text{Charge energy}} \times 100\% \tag{12}$$

$$VE = \frac{EE}{CE} \times 100\% \tag{13}$$

3. Results and discussion

3.1. Characterization of HCSNs

SEM and TEM images of the HCSNs are displayed in Fig. 1. In Fig. 1(b), carbon nanospheres with apparent notches clearly indicate the cavity in the HCSNs. Only the elements C and O were detected via EDX spectroscopy (Fig. S1 in Appendix A). The uniform particle size of the HCSNs can be observed in Fig. 1(b). However, the analyzed particle sizes of the HCSNs via a zeta potentiometer ranged from 220 to 530 nm (Fig. 1(c)), which can be ascribed to the inevitable agglomeration of the HCSNs, leading to larger particle size test values. The TEM micrograph (Fig. 1(d)) clearly shows the sharp contrast between the dark edge and light-colored center of the HCSNs, confirming the hollow nature of the carbon spheres. The thickness of the carbon shell was about 80 nm (one-fifth of the entire diameter) and the size of the HCSNs as measured from the TEM micrograph was in good agreement with the SEM characterization results. The FT-IR spectra of the HCSNs are displayed in Fig. S2 in Appendix A, where the characteristic band at 3415 cm^{-1} belongs to the stretching vibration of the hydroxyl group (OH) [40]; the wagging vibration peak of the hydroxyl group also appears at 665 cm^{-1}, indicating abundant hydrophilic groups on the surface of the HCSNs. The absorption peak of the carbon spheres appears at 1630 cm^{-1} (the C=O stretching of the –COOH groups) and the –COOH peak appears at 1271 cm^{-1}. The X-ray

photoelectron spectroscopy (XPS) C 1s spectra of the HCSNs further proves the existence of hydrophilic groups (Fig. 1(e)). The pore size distribution of the HCSNs was analyzed using the Horvath–Kawazoe method and tested via nitrogen adsorption–desorption. The nitrogen adsorption–desorption isotherm of HCSNs is shown in Fig. S3 in Appendix A, and the Brunauer–Emmett–Teller (BET) specific surface area of the HCSNs was found to be 1023 $m^2 \cdot g^{-1}$. Nanosized micropores were detected on the walls of the carbon spheres (Fig. 1(f)), exhibiting a micropore size distribution of approximately 0.62 nm. In addition, the HCSN powder well maintained its initial architecture and morphology after being immersed in 3 $mol \cdot L^{-1}$ sulfuric acid solution for 30 days at room temperature, indicating excellent structural stability in a strong acid environment (Fig. S4 in Appendix A).

3.2. Membrane morphologies and characterizations

SPEEK membranes embedded with different HCSN contents were then fabricated via the solution casting method. The membranes were denoted as S/HCSN-*Y*, where "S" stands for SPEEK with a sulfonation degree of about 67% (Fig. S5 in Appendix A), and *Y* represents the weight ratio of the HCSNs in the SPEEK matrix. As shown in the digital photos, the color of the membranes became darker as the loading content of the HCSNs increased (Fig. 1(g) and Fig. S6 in Appendix A). Table S1 in Appendix A presented the initial higher transmittance of characteristic bands at 1635 and 1278 cm^{-1} belonging to hydrophilic oxygen-containing groups of HCSNs for hybrid membranes with loadings of 1–3 (S/HCSN-1, -2, and -3), compared with SPEEK membrane. The later lower transmittance can be ascribed to the deeper black of hybrid membranes. Thus, this trend demonstrated the successful incorporation of HCSNs into the polymer matrix. The HCSNs had little influence on the chemical structure of the SPEEK polymer (Fig. S7 in Appendix A). The SEM results showed that the surfaces of both the pristine membrane and the hybrid membranes were flat (Fig. S8 in Appendix A). Compared with the pristine membrane, the network structure of the hybrid membranes was uniformly filled with HCSNs; as the HCSN content increased, the distribution of HCSNs became increasingly denser in each grid (Fig. S9 in Appendix A). The EDX mapping results of the cross-section SEM image of the S/HCSN-3 membrane demonstrated the existence of the elements C, O, and S in the hybrid membrane; the hybrid membrane did not contain any other impurities (Fig. S10 in Appendix A). Figs. 1(h) and (i) show the good interfacial compatibility between the fillers and the polymer. However, aggregation of the HCSNs occurred easily at high loadings of 4% and 5% (w/w), as shown in Fig. S11 in Appendix A. A white light interferometer (Fig. S12 in Appendix A) demonstrated that the surface of the hybrid membranes with higher loadings of 4% and 5% (w/w) had become rough and contained some humps (originating from the HCSNs). In particular, round spots were observed on the relatively smooth polymer surface of the S/HCSN hybrid membranes, increasing the surface roughness of the original SPEEK membrane. XRD patterns demonstrated enhanced crystallinity of the hybrid membranes, due to interactions between the HCSNs and the polymer (Fig. S13 in Appendix A). The thermal stabilities of the hybrid membranes were measured via TG analysis (Fig. S14 in Appendix A); it was found that the introduction of HCSNs into the polymer resulted in a significant improvement of the thermal stability of the hybrid membrane.

3.3. WU, SR, and IEC

The WU and SR have a crucial influence on the performance of a membrane, as the WU affects the proton transmission capacity, and the higher SR of the membrane lowers the dimensional stability, increasing the membrane's permeability to vanadium ions [41]. Compared with the pristine SPEEK membrane, all the hybrid membranes had a higher water absorption ability (Fig. 2(a)). As the concentration of the HCSN nanofillers increased, the WU of the S/HCSN hybrid membranes increased from 31.9% to 36.9%, due to the hydrophilic micropores on the surface of the HCSNs (Fig. 1(f) and Fig. S2) and the accessible internal cavities (Fig. 1(d)). However, when the loading amount exceeded 3% (w/w), the inevitable agglomeration between the HCSNs in the polymer matrix sacrificed part of the water absorption ability, resulting in a lower WU for the hybrid membranes with loadings of 4% and 5% (w/w) (S/HCSN-4 and -5), compared with that of the S/HCSN-3 membrane. Fig. S15 in Appendix A presents the results for the water contact angle measurement on the surface of the pristine and hybrid membranes as-prepared membranes. The surfaces of the hybrid membranes were clearly more hydrophilic with a smaller water contact angle, in comparison with the pristine membrane; these findings were consistent with the surface roughness results for the various membranes, as reported above.

Although the WU of the SPEEK membranes embedded with nanofillers was improved, the SR of the hybrid membranes was lower than that of the pristine membrane (Fig. 2(a)). On the one hand, the uniformly distributed HCSNs effectively inhibited the movement of the polymer chains, thereby reducing the degree of extension of the membrane size after water absorption. On the other hand, hydrogen-bonding interactions between the hydrophilic groups of the HCSNs and the sulfonic acid group of SPEEK resulted in a decline in the SR of the membrane. Among the hybrid membranes, the S/HCSN-3 hybrid membrane had the highest WU and a relatively low SR—values far superior to those of the commercial Nafion 212 (N212) membrane (Fig. S16 in Appendix A). In addition, the IECs of the hybrid membranes were higher than that of the SPEEK membrane (Fig. S17 in Appendix A), which was basically consistent with the test results for WU.

3.4. Oxidative stability and mechanical properties

It is well known that chemical stability is critical for hydrocarbon membranes such as SPEEK because of the strong oxidation of the VO_2^+ catholyte in VFBs [42]. The hybrid membranes with different HCSN loading contents, a pristine membrane, and an N212 membrane were immersed in 0.1 $mol \cdot L^{-1}$ VO_2^+ electrolyte. During the first week, all the membranes showed good stability (Fig. S18(a) in Appendix A). Over time, the hybrid membranes exhibited superior chemical stability in comparison with the pristine membrane. The reduction of VO_2^+ to VO^{2+} was much lower for the hybrid membranes than for the pure SPEEK membrane, demonstrating that the introduction of HCSNs effectively mitigates the degradation process of the hydrocarbon membrane and provides better durability for practical applications (Fig. S18(b) in Appendix A). Although the reduction of VO_2^+ to VO^{2+} was higher for our membranes than for N212, the appropriate HCSN content plays a significant role in the protection of the SPEEK matrix, and the degradation rate of our membranes is close to that of N212. This protection may be attributed to the weakened protonation of the oxygen atom in the ether bond of the SPEEK main chains due to the H^+ absorption by the HCSNs, hydrogen-bonding interactions, and the additional physical barrier of the HCSNs.

The high mechanical strength of the membrane is a key performance parameter for VFBs, especially for the long charge–discharge cycles. As shown in Fig. 2(b), the HCSNs had a significant enhancement effect on the base membrane. In particular, with a nanofiller loading of 3% (w/w), S/HCSN-3 exhibited the highest tensile strength (35.8 MPa), which was nearly two times greater than that of the pure membrane (19.5 MPa). Compared with the N212 membrane (21.8 MPa), the optimized membrane still had an advantage in this respect (Fig. S19 in Appendix A). Good durability

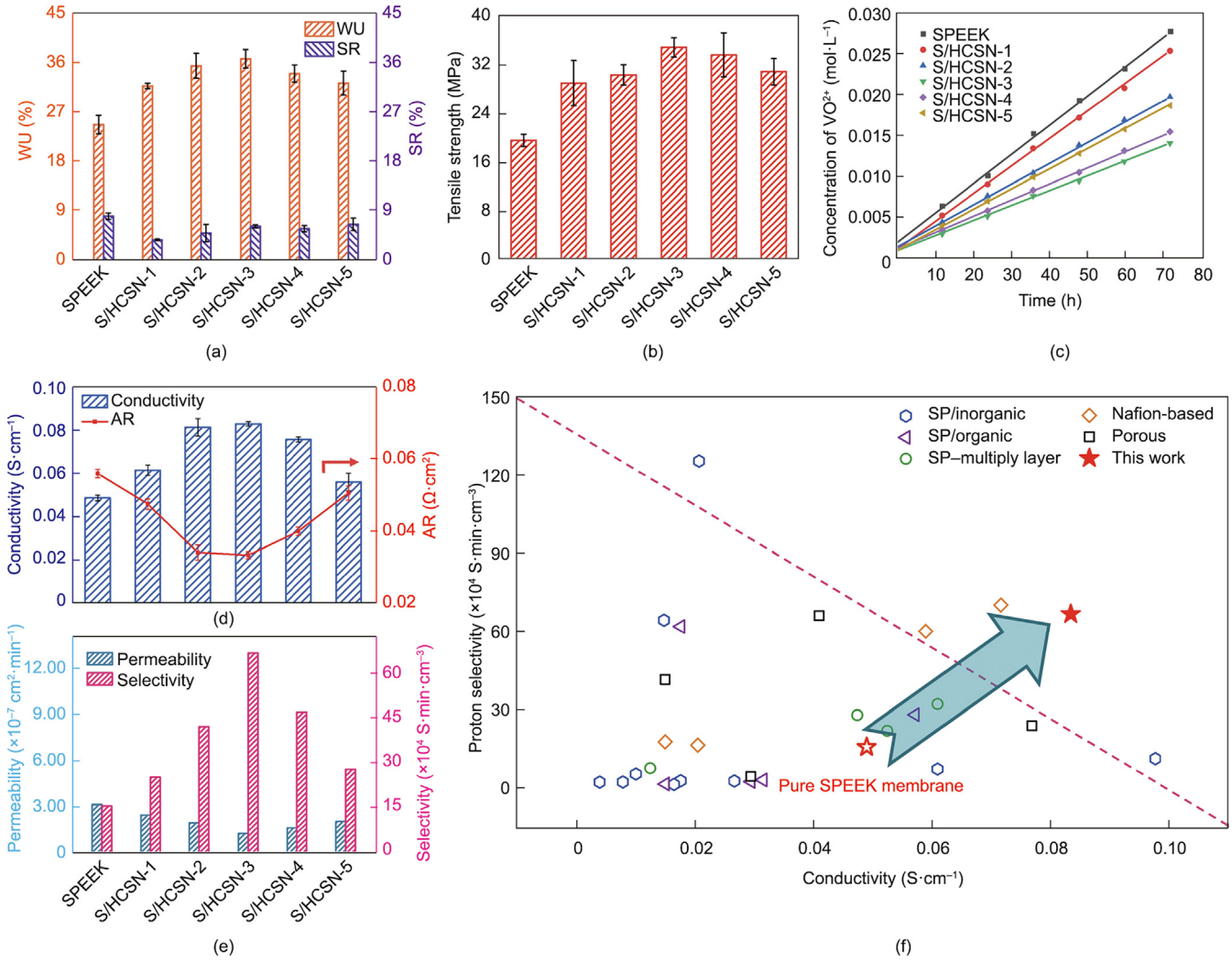

Fig. 2. Physicochemical properties of different membranes. (a) WU and SR; (b) tensile strength; (c) concentration change of VO^{2+} species versus time in the $MgSO_4$ compartment; (d) conductivity and AR; (e) VO^{2+} permeability and selectivity; (f) plot of the proton selectivity versus conductivity of various membranes for VFBs reported in recent years; detailed legends are as follows. SP/inorganic: SPEEK hybrid membranes embedded with inorganic fillers; SP/organic: SPEEK membranes blended with polymers; SP–multiply layer: SPEEK composite membranes protected by inert films or coatings; Nafion-based: Nafion membranes modified by various methods; porous: porous membranes created using phase separations.

enhances the membrane's resistance to undesirable effects caused by electrolyte cyclic flushing. This is beneficial to the long-term operation of the membrane, as it extends the running time of the membrane and the use lifespan of the VFB.

3.5. Proton selectivity and conductivity

A membrane with a strong ability to hamper active vanadium species brings considerable benefit to a VFB, in that it can mitigate the capacity fading of the battery and provide high CE values. As shown in Fig. 2(c), the growth rate of the vanadium ion concentration of the S/HCSN hybrid membranes was significantly lower than that of the pure membrane, indicating that the HCSNs served as an effective physical barrier to the diffusion of vanadium ions in the polymer matrix, thereby increasing the membranes' penetration resistance to vanadium ions. However, it was not the case that the greater the HCSN content, the better the effect. When the loading amount exceeded 3% (w/w), the vanadium ion permeability of the membrane began to increase, because a too-large amount of HCSNs resulted in aggregation and uneven dispersion in the SPEEK matrix.

The AR and conductivity of various membranes are presented in Fig. 2(d). With the introduction of HCSNs, the AR of the membranes was significantly reduced. Moreover, the AR values for the hybrid membranes with increasing HCSN loading first declined and then rose in comparison with that of the pure membrane. In contrast, the proton conductivity exhibited an opposite trend as the loading content increased. The initial higher proton conductivity can be attributed to the shorter internal proton-transfer pathway, as the nanofillers possess three-dimensional (3D) hollow structures, while the later lower proton conductivity can be attributed to the partial increase in resistance resulting from the inevitable agglomeration of HCSNs at higher loadings. As a result, the S/HCSN-3 membrane exhibited the highest proton conductivity (0.084 $S \cdot cm^{-1}$ at 25 °C) in comparison with the pure membrane (0.049 $S \cdot cm^{-1}$) and the N212 membrane (0.033 $S \cdot cm^{-1}$).

Proton selectivity, which in this context is defined as the ratio of proton conductivity to vanadium ion permeability (H/V), is a key factor in estimating the overall performance of a VFB. Fig. 2(e) shows that the S/HCSN-3 membrane displayed superior H/V selectivity (6.68×10^5 $S \cdot min \cdot cm^{-3}$) among various membranes, with a selectivity approximately 4.3 times higher than that of the SPEEK membrane (1.56×10^5 $S \cdot min \cdot cm^{-3}$). In addition, the proton

selectivity of the optimized membrane was about 5.9-fold greater than that of the N212 membrane (1.13×10^5 S·min·cm^{-3}) under the same measurement conditions (Fig. S20 in Appendix A). More importantly, Fig. 2(f) and Table S2 in Appendix A show the ultrahigh proton selectivity and proton conductivity of the S/HCSN-3 membrane in comparison with those of other reported membranes for VFBs, which are due to the contribution of the HCSNs. Therefore, VFBs assembled with the S/HCSN-3 membrane are expected to show excellent cell performance.

3.6. VFB single cell performance

A series of prepared membranes were assembled for a VFB single cell to measure their charge–discharge performance at current densities ranging from 40 to 120 mA·cm^{-2}. As shown in Fig. S21 in Appendix A, with all the tested membranes, the cell possessed increased CE but decreased VE with increased current density. The former can be ascribed to the shorter time to a charge and discharge cycle, which gives rise to more moderate vanadium ion crossover. The latter is due to the higher overpotential and ohmic polarization when the applied current density increases [43]. On the whole, the cell performance of the SPEEK membrane was enhanced by the incorporation of the HCSN nanofillers; in particular, the S/HCSN-3 membrane exhibited the best battery performance.

In order to further present the performance advantages of the S/HCSN-3 membrane, a commercial N212 membrane was used as a benchmark for comparison, as this commercial membrane has universal practicability in VFBs and has better battery performance than other commercial membranes such as Nafion 115 (Fig. S22 in Appendix A). Fig. 3(a) displays the battery performance of a

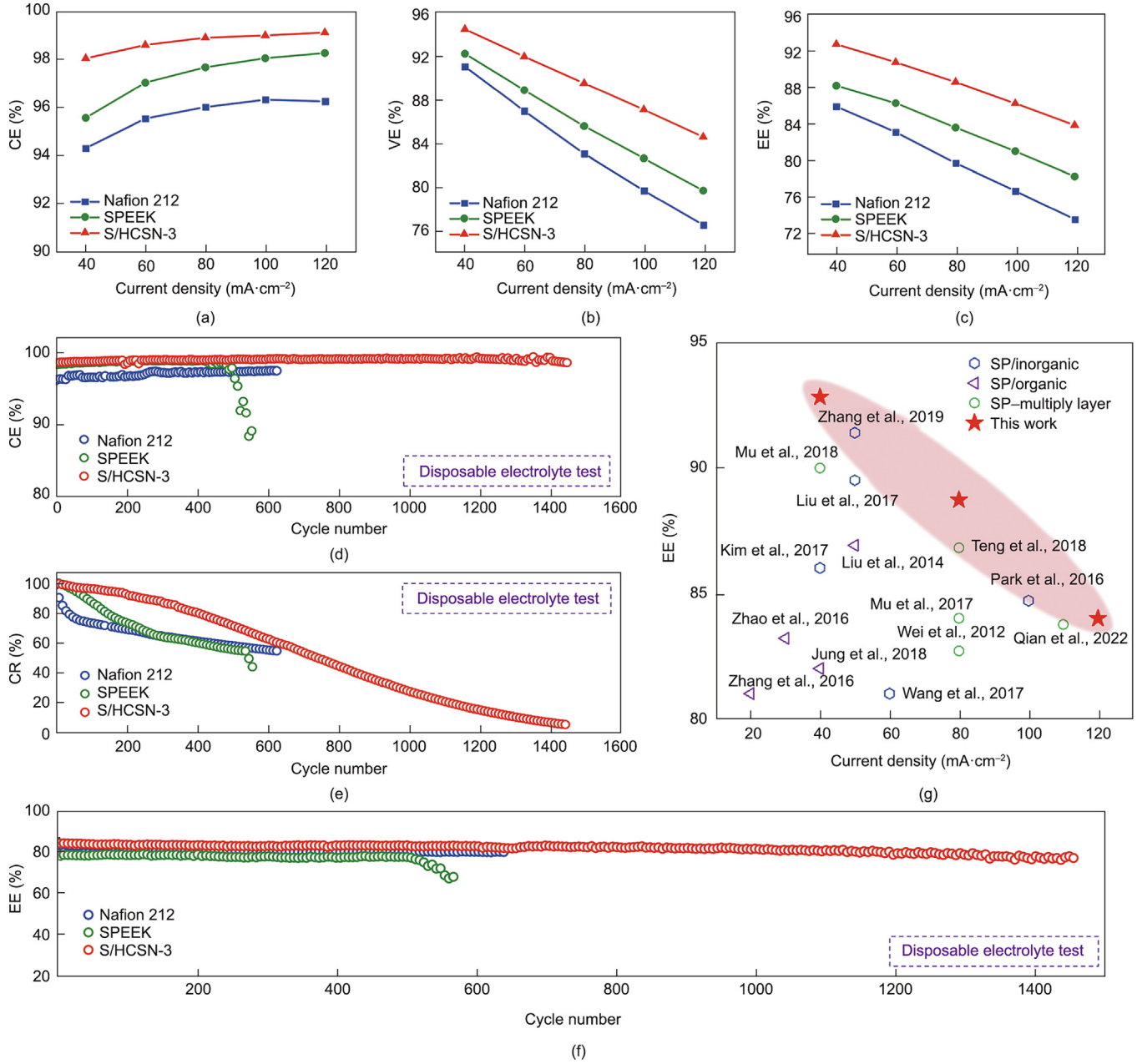

Fig. 3. Battery performance. (a–c) Comparison of VFB efficiencies with the N212, SPEEK, and S/HCSN-3 membranes: (a) CE, (b) VE, and (c) EE at 40–120 mA·cm^{-2}. (d–f) Long-term cycling stability test of VFBs with the N212, SPEEK, and S/HCSN-3 membranes utilizing disposable electrolyte at 120 mA·cm^{-2}: (d) CE; (e) capacity retention (CR); (f) EE. (g) Comparison of the EEs of VFBs assembled with various types of modified SPEEK-based membranes in recent years (corresponding data were listed in Table S3 in Appendix A).

VFB single cell with the N212, SPEEK, and S/HCSN-3 membranes, respectively, at different current densities. Compared with the other membranes, the CEs of the VFB with the S/HCSN-3 membrane continuously maintained the highest level. The S/HCSN-3 membrane had a longer self-discharge voltage holding time (73 h) than the N212 membrane (40 h) and the SPEEK membrane (53 h), indicating that it more effectively hinders the crossover of vanadium ions (Fig. S23 in Appendix A), which is consistent with the results of the permeability test discussed earlier (Fig. S20). In addition, benefiting from its considerately higher proton conductivity, the S/HCSN-3 membrane retained a higher VE value (94.6% at 40 $mA{\cdot}cm^{-2}$ and 84.7% at 120 $mA{\cdot}cm^{-2}$) than the SPEEK or N212 membranes (Fig. 3(b)). The peak power density of the cell with the S/HCSN-3 membrane reached 400.8 $mW{\cdot}cm^{-2}$, in comparison with 352.7 and 383.2 $mW{\cdot}cm^{-2}$ for the cells with the N212 and SPEEK membranes, respectively (Fig. S24 in Appendix A). This result suggests that the HCSNs do indeed boost the speed of proton transport within the hybrid membranes [44]. Since the CEs and VEs jointly determine the value of the EE performance, the best EEs were realized with the S/HCSN-3 membrane (Fig. 3(c)). Fig. S25 in Appendix A compares the charge–discharge curves of the VFBs assembled with the N212, SPEEK, and S/HCSN-3 membranes at 40–120 $mA{\cdot}cm^{-2}$. The specific volume discharge capacity of the cell with the S/HCSN-3 membrane (20.9 $A{\cdot}h{\cdot}L^{-1}$) is higher than those with the N212 membrane (16.2 $A{\cdot}h{\cdot}L^{-1}$) and the SPEEK membrane (18.6 $A{\cdot}h{\cdot}L^{-1}$) at a current density of 120 $mA{\cdot}cm^{-2}$.

The lifespan of the ICM is an extremely significant technical indicator during the working process of a VFB, especially for practical applications. As shown in Fig. 3(d), the cell assembled with the S/HCSN-3 membrane exhibited an initial CE of 98.8% at a high current density of 120 $mA{\cdot}cm^{-2}$ and maintained a high and stable level (about 99.6% after 1450 cycles), while that assembled with the SPEEK membrane showed a sharp decline after 510 cycles (only 96.4% at that point). Fig. S26 in Appendix A also shows the intact membrane structure of the S/HCSN-3 membrane after more than 1400 cycles. Thus, this test well proved that both the chemical stability and the mechanical strength of the membranes were significantly reinforced by combining a pristine membrane with HCSNs.

It should be noted that the positive and negative electrolytes were not refreshed during the tests. Among these three kinds of membranes, the water migration of the cells equipped with the N212 membrane become exceptionally rapid, resulting in relatively low cycle numbers (630 cycles). In comparison, our S/HCSN-3 membrane did a good job in retarding active vanadium species crossover and inhibiting water migration, with an average discharge capacity decay of only 0.065% per cycle, showing a strong advantage over the original membrane (0.12% per cycle), as displayed in Fig. 3(e). In addition to a longer running time, the EE values of the S/HCSN-3 membrane maintained a relatively high level (over 80%), which was higher than that of the pure SPEEK (initial EE of 78.1%) (Fig. 3(f)). After 100 cycles, these difference in the cycling performance of VFB at 120 $mA{\cdot}cm^{-2}$ became clearer, as the S/HCSN-3 membrane showed a higher EE performance and lower discharge capacity decay in comparison with the other membranes (Fig. S27 in Appendix A). As shown in Fig. S28 in Appendix A, the S/HCSN-3 membrane demonstrated a superior battery performance and more reliable cycle stability than the SPEEK membrane under 160 $mA{\cdot}cm^{-2}$. It is also worth noting that the EEs of the VFBs equipped with the S/HCSN-3 membrane in this work are superior to those in most of the reported works about SPEEK-based membranes (Fig. 3(g) and Table S3 in Appendix A).

3.7. Contributions of the HCSNs

The above results demonstrate that the introduction of HCSNs into the polymer matrix is a feasible strategy to fabricate high-performance ICMs. To further illustrate the contributions of the HCSNs to the hybrid membranes, additional experiments were carried out. Fig. 4(a) represents the vanadium ion permeability of membranes containing 1%–3% (w/w) of solid carbon nanospheres (SCNs). The corresponding membranes are denoted as S/SCN-1, S/SCN-2, and S/SCN-3. All three have a vanadium resistance similar to those of their S/HCSN counterparts, confirming that the HCSNs have equally good ion-sieving ability as the SCNs. The intrinsic transport behaviors of VO^{2+} in the nanofillers (both SCNs and HCSNs) were analyzed qualitatively using the Maxwell model based on experimental permeability data (Fig. 4(b)) [45]. The fitting results indicated the similar permeability of the two types of carbon nanospheres to the active vanadium species, exhibiting the precise ion sieving at the surface of the HCSNs. In contrast, a sharp decrease in proton conductivity was observed for the S/SCN membranes, which can be ascribed to the internal ultrafast proton transport pathways of the HCSNs.

LF-NMR was employed to detect and characterize the proton transport channels within the S/HCSN membranes, using water as a probe molecule (Fig. 4(c)). The transverse relaxation time represents the degree of water molecule confinement inside the space [46,47]. Three peaks (I, II, and III) appeared for both the SPEEK and S/HCSN-3 membranes. Peak I (which appears at a low relaxation time) for the SPEEK membrane is indicative of water molecules penetrating the sub-nanometer space derived from the tangling of random polymer chains. Fig. S29 in Appendix A demonstrates this point; moreover, more serious swelling behavior is observed within N212. For the S/HCSN-3 membrane, the shift of peak I to an upward relaxation time and the increase of population in the sub-nanometer confined relaxation time indicate the hydrophilic micropore structure on the surface of HCSNs [48], which is consistent with the measurement results shown in Fig. 1(f) and Fig. S2. The peak II (which exists in the moderate relaxation time) area ratio for the S/HCSN-3 membrane sharply rises to 40.22% compared with that of the pristine membrane (10.03%), demonstrating that the internal cavities of the HCSNs result in the formation of more abundant nanoconfined transport channels, favoring an improvement in the WU and IEC of the hybrid membranes (Fig. 2(a) and Fig. S17). These nanoconfined transport channels without resistance greatly facilitate the proton transfer (Fig. 4(c)).

4. Conclusions

This work successfully demonstrated the utilization of a polymeric membrane embedded with HCSNs for VFBs. The physiochemical properties of the hybrid membrane, such as its mechanical strength, chemical stability, and WU, were greatly enhanced by the incorporation of HCSNs. Furthermore, the hybrid membrane exhibited superior conductive proton selectivity due to the size exclusion effect of the microporous shell and the reduced resistance to proton transport in the internal cavity of the HCSNs. The VFB with the optimized membrane presented a more desirable electrochemical performance in comparison with those of commercial N212 and pure SPEEK membranes. A cell based on the optimized S/HCSN-3 membrane exhibited a higher CE and comparable EE during a charge–discharge process of more than 1400 cycles (over 475 h)—much longer than those of the N212 (260 h) and SPEEK (207 h) membranes—at 120 $mA{\cdot}cm^{-2}$. This work demonstrates that the proposed hybrid membrane is a promising

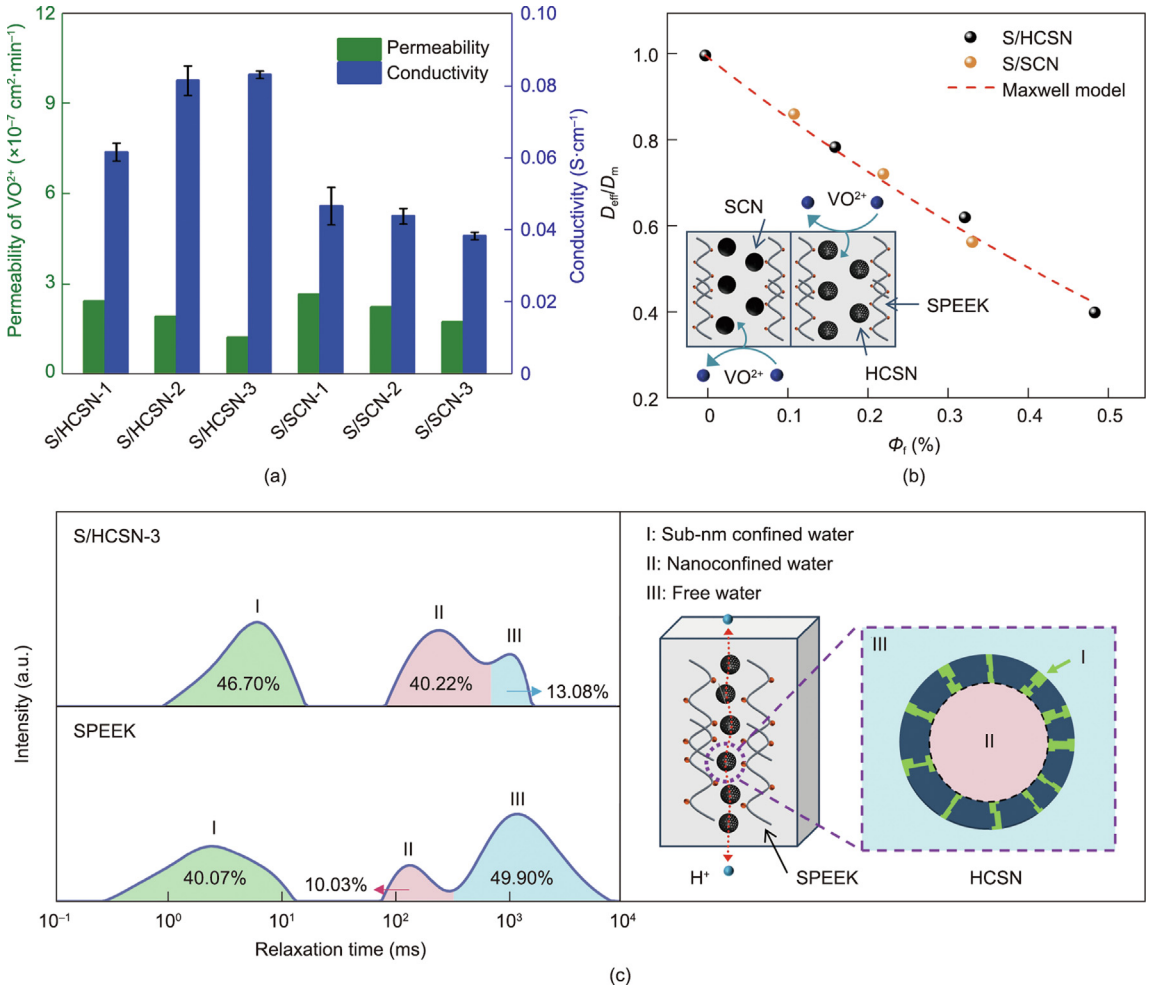

Fig. 4. Roles of HCSNs in the hybrid membranes. (a) Comparison of the VO^{2+} permeability and proton conductivity of the S/HCSN and S/SCN membranes. (b) Comparison of the D_{eff}/D_m of the S/HCSN and S/SCN membranes between the experimental VO^{2+} permeability data and the Maxwell model prediction at different filler volume fractions. (c) LF-NMR spectra of the SPEEK and S/HCSN-3 membranes and schematic illustration of the confinement space forming proton transport channels within the S/HCSN membranes. nm: nanometer.

candidate for commercial application in next-generation VFBs for large-scale energy storage.

Acknowledgments

The authors appreciate the support from the National Key Research and Development Program of China (2021YFB3801301), the National Natural Science Foundation of China (22075076, 21908098, and 21908054), and the Priority Academic Program Development of Jiangsu Higher Education Institutions (PAPD). Thanks to eceshi (www.eceshi.com) for the LF-NMR analysis.

Compliance with ethics guidelines

Kang Huang, Shuhao Lin, Yu Xia, Yongsheng Xia, Feiyan Mu, Yuqin Lu, Hongyan Cao, Yixing Wang, Weihong Xing, and Zhi Xu declare that they have no conflict of interest or financial conflicts to disclose.

Data availability statement

The data supporting the findings of this study are available from the corresponding author upon reasonable request.

Appendix A. Supplementary data

Supplementary data to this article can be found online at https://doi.org/10.1016/j.eng.2022.11.008.

References

[1] Gür TM. Review of electrical energy storage technologies, materials and systems: challenges and prospects for large-scale grid storage. Energy Environ Sci 2018;11(10):2696–767.
[2] Zeng Q, Lai Y, Jiang L, Liu F, Hao X, Wang L, et al. Integrated photorechargeable energy storage system: next-generation power source driving the future. Adv Energy Mater 2020;10(14):1903930.
[3] Tan KM, Babu TS, Ramachandaramurthy VK, Kasinathan P, Solanki SG, Raveendran SK. Empowering smart grid: a comprehensive review of energy storage technology and application with renewable energy integration. J Energy Storage 2021;39:102591.
[4] Liu J, Wang Q, Song Z, Fang F. Bottlenecks and countermeasures of high-penetration renewable energy development in China. Engineering 2021;7(11):1611–22.
[5] Zhang S, Chen W. China's energy transition pathway in a carbon neutral vision. Engineering 2022;14:64–76.
[6] Zhang XQ, Zhao CZ, Huang JQ, Zhang Q. Recent advances in energy chemical engineering of next-generation lithium batteries. Engineering 2018;4(6):831–47.
[7] Du S. Recent advances in electrode design based on one-dimensional nanostructure arrays for proton exchange membrane fuel cell applications. Engineering 2021;7(1):33–49.
[8] Xia Y, Wang Y, Cao H, Lin S, Xia Y, Hou X, et al. Rigidly and intrinsically microporous polymer reinforced sulfonated polyether ether ketone membrane for vanadium flow battery. J Membr Sci 2022;653:120517.

[9] Zuo P, Li Y, Wang A, Tan R, Liu Y, Liang X, et al. Sulfonated microporous polymer membranes with fast and selective ion transport for electrochemical energy conversion and storage. Angew Chem Int Ed Engl 2020;59(24):9564–73.
[10] Cao H, Xia Y, Lu Y, Wu Y, Xia Y, Hou X, et al. MOF-801 polycrystalline membrane with sub-10 nm polymeric assembly layer for ion sieving and flow battery storage. AIChE J 2022;68(6):e17657.
[11] Xu T, Wu B, Hou L, Zhu Y, Sheng F, Zhao Z, et al. Highly ion-permselective porous organic cage membranes with hierarchical channels. J Am Chem Soc 2022;144(23):10220–9.
[12] Wang W, Zhang Y, Yang X, Sun H, Wu Y, Shao L. Monovalent cation exchange membranes with Janus charged structure for ion separation. Engineering. Forthcoming 2023.
[13] Zhang D, Xin L, Xia Y, Dai L, Qu K, Huang K, et al. Advanced Nafion hybrid membranes with fast proton transport channels toward high-performance vanadium redox flow battery. J Membr Sci 2021;624:119047.
[14] Ye J, Zhao X, Ma Y, Su J, Xiang C, Zhao K, et al. Hybrid membranes dispersed with superhydrophilic TiO_2 nanotubes toward ultra-stable and high-performance vanadium redox flow batteries. Adv Energy Mater 2020;10(22):1904041.
[15] Dai Q, Xing F, Liu X, Shi D, Deng C, Zhao Z, et al. High-performance PBI membranes for flow batteries: from the transport mechanism to the pilot plant. Energy Environ Sci 2022;15(4):1594–600.
[16] Yuan Z, Liang L, Dai Q, Li T, Song Q, Zhang H, et al. Low-cost hydrocarbon membrane enables commercial-scale flow batteries for long-duration energy storage. Joule 2022;6(4):884–905.
[17] Lou X, Lu B, He M, Yu Y, Zhu X, Peng F, et al. Functionalized carbon black modified sulfonated polyether ether ketone membrane for highly stable vanadium redox flow battery. J Membr Sci 2022;643:120015.
[18] Zhang Y, Wang H, Qian P, Zhou Y, Shi J, Shi H. Sulfonated poly(ether ether ketone)/amine-functionalized graphene oxide hybrid membrane with various chain lengths for vanadium redox flow battery: a comparative study. J Membr Sci 2020;610:118232.
[19] Zeng L, Ye J, Zhang J, Liu J, Jia C. A promising SPEEK/MCM composite membrane for highly efficient vanadium redox flow battery. Surf Coat Tech 2019;358:167–72.
[20] Dai L, Xu F, Huang K, Xia Y, Wang Y, Qu K, et al. Ultrafast water transport in two-dimensional channels enabled by spherical polyelectrolyte brushes with controllable flexibility. Angew Chem Int Ed Engl 2021;60(36):19933–41.
[21] Xin L, Zhang D, Qu K, Lu Y, Wang Y, Huang K, et al. Zr-MOF-enabled controllable ion sieving and proton conductivity in flow battery membrane. Adv Funct Mater 2021;31(42):2104629.
[22] Kim J, Han J, Kim H, Kim K, Lee H, Kim E, et al. Thermally cross-linked sulfonated poly(ether ether ketone) membranes containing a basic polymer-grafted graphene oxide for vanadium redox flow battery application. J Energy Storage 2022;45:103784.
[23] Ji Y, Tay ZY, Li SFY. Highly selective sulfonated poly(ether ether ketone)/titanium oxide composite membranes for vanadium redox flow batteries. J Membr Sci 2017;539:197–205.
[24] Hyeon DH, Chun JH, Lee CH, Jung HC, Kim SH. Composite membranes based on sulfonated poly(ether ether ketone) and SiO_2 for a vanadium redox flow battery. Korean J Chem Eng 2015;32(8):1554–63.
[25] Aziz MA, Shanmugam S. Ultra-high proton/vanadium selectivity of a modified sulfonated poly(arylene ether ketone) composite membrane for all vanadium redox flow batteries. J Mater Chem A 2017;5(32):16663–71.
[26] Lim DW, Kitagawa H. Proton transport in metal–organic frameworks. Chem Rev 2020;120(16):8416–67.
[27] Pachfule P, Acharjya A, Roeser J, Langenhahn T, Schwarze M, Schomäcker R, et al. Diacetylene functionalized covalent organic framework (COF) for photocatalytic hydrogen generation. J Am Chem Soc 2018;140(4):1423–7.
[28] Guo ZC, Shi ZQ, Wang XY, Li ZF, Li G. Proton conductive covalent organic frameworks. Coord Chem Rev 2020;422:213465.
[29] Zhang Z, Cui X, Jiang X, Ding Q, Cui J, Zhang Y, et al. Efficient splitting of *trans*-/*cis*-olefins using an anion-pillared ultramicroporous metal–organic framework with guest-adaptive pore channels. Engineering 2022;11:80–6.
[30] Wang X, Ding X, Zhao H, Fu J, Xin Q, Zhang Y. Pebax-based mixed matrix membranes containing hollow polypyrrole nanospheres with mesoporous shells for enhanced gas permeation performance. J Membr Sci 2020;602:117968.
[31] Liu W, Luo N, Li P, Yang X, Dai Z, Song S, et al. New sulfonated poly (ether ether ketone) composite membrane with the spherical bell-typed superabsorbent microspheres: excellent proton conductivity and water retention properties at low humidity. J Power Sources 2020;452:227823.
[32] Wang J, Liu Y, Cai Q, Dong A, Yang D, Zhao D. Hierarchically porous silica membrane as separator for high-performance lithium-ion batteries. Adv Mater 2022;34(3):2107957.
[33] Lee JH, Im K, Han S, Yoo SJ, Kim J, Kim JH. Bimodal-porous hollow MgO sphere embedded mixed matrix membranes for CO_2 capture. Separ Purif Tech 2020;250:117065.
[34] Liu WY, Ju XJ, Pu XQ, Cai QW, Liu YQ, Liu Z, et al. Functional capsules encapsulating molecular-recognizable nanogels for facile removal of organic micro-pollutants from water. Engineering 2021;7(5):636–46. Corrigendum in: Engineering 2021;7(9):1342.
[35] Zhang J, Schott JA, Li Y, Zhan W, Mahurin SM, Nelson K, et al. Membrane-based gas separation accelerated by hollow nanosphere architectures. Adv Mater 2017;29(4):1603797.
[36] Salahshoor Z, Shahbazi A, Koutahzadeh N. Developing a novel nitrogen-doped hollow porous carbon sphere (N-HPCS) blended nanofiltration membrane with superior water permeance characteristic for high saline and colored wastewaters treatment. Chem Eng J 2022;431(Pt 2):134068.
[37] Park SS, Rieth AJ, Hendon CH, Dincă M. Selective vapor pressure dependent proton transport in a metal–organic framework with two distinct hydrophilic pores. J Am Chem Soc 2018;140(6):2016–9.
[38] Petersen MK, Voth GA. Characterization of the solvation and transport of the hydrated proton in the perfluorosulfonic acid membrane Nafion. J Phys Chem B 2006;110(37):18594–600.
[39] Dai Q, Liu Z, Huang L, Wang C, Zhao Y, Fu Q, et al. Thin-film composite membrane breaking the trade-off between conductivity and selectivity for a flow battery. Nat Commun 2020;11(1):13. Corrected in: Nat Commun 2020;11(1):2609.
[40] Ye J, Cheng Y, Sun L, Ding M, Wu C, Yuan D, et al. A green SPEEK/lignin composite membrane with high ion selectivity for vanadium redox flow battery. J Membr Sci 2019;572:110–8.
[41] Li A, Wang G, Wei X, Li F, Zhang M, Zhang J, et al. Highly selective sulfonated poly(ether ether ketone)/polyvinylpyrrolidone hybrid membranes for vanadium redox flow batteries. J Mater Sci 2020;55(35):16822–35.
[42] Yuan Z, Li X, Hu J, Xu W, Cao J, Zhang H. Degradation mechanism of sulfonated poly(ether ether ketone) (SPEEK) ion exchange membranes under vanadium flow battery medium. Phys Chem Chem Phys 2014;16(37):19841–7.
[43] Zhao Y, Zhang H, Xiao C, Qiao L, Fu Q, Li X. Highly selective charged porous membranes with improved ion conductivity. Nano Energy 2018;48:353–60.
[44] Ye J, Zheng C, Liu J, Sun T, Yu S, Li H. *In situ* grown tungsten trioxide nanoparticles on graphene oxide nanosheet to regulate ion selectivity of membrane for high performance vanadium redox flow battery. Adv Funct Mater 2022;32(8):2109427.
[45] Vinh-Thang H, Kaliaguine S. Predictive models for mixed-matrix membrane performance: a review. Chem Rev 2013;113(7):4980–5028.
[46] Zhang WH, Yin MJ, Zhao Q, Jin CG, Wang N, Ji S, et al. Graphene oxide membranes with stable porous structure for ultrafast water transport. Nat Nanotechnol 2021;16(3):337–43.
[47] Li X, Wang Y, Chang J, Sun H, He H, Qian C, et al. "Mix-then-on-demand-complex": *in situ* cascade anionization and complexation of graphene oxide for high-performance nanofiltration membranes. ACS Nano 2021;15(3):4440–9.
[48] Ji YL, Gu BX, Xie SJ, Yin MJ, Qian WJ, Zhao Q, et al. Superfast water transport zwitterionic polymeric nanofluidic membrane reinforced by metal–organic frameworks. Adv Mater 2021;33(38):2102292.